Radical Reactions with Organic Thin Films: Chemical Interaction of Atomic Oxygen with an X-ray Modified Self-Assembled Monolayer

Jessica Torres, Christopher C. Perry, Stephen J. Bransfield, and D. Howard Fairbrother*

Department of Chemistry, The Johns Hopkins University, 3400 N. Charles Street, Baltimore, Maryland 21218

Received: March 6, 2002; In Final Form: May 5, 2002

The interaction of an X-ray-modified self-assembled monolayer with a mixture of atomic and molecular oxygen (O/O_2) has been studied using in situ X-ray photoelectron spectroscopy. Initially the reaction dynamics are dominated by the incorporation of new oxygen containing functionality at the vacuum/film interface. At intermediate O/O_2 exposures, when a steady-state concentration of C−O, C═O, and O−C═O groups has been established, the production of volatile carbon-containing species, including CO_2, is responsible for etching the hydrocarbon film. Upon prolonged O/O_2 exposures, O atoms penetrate to the film/substrate interface, producing Au_2O_3 and sulfonate (RSO_3) species. Under steady-state conditions, the thickness of the hydrocarbon film was reduced with an efficiency of $\approx 7.4 \times 10^{-4}$ Å/impingent O atom while the average penetration depth of O atoms within the hydrocarbon film was determined to be ≈5.5 Å.

Introduction

Oxygen plasmas play an important role in the modification of polymer surfaces based on their ability to introduce new functionalities at the interface, thereby changing a material's surface properties.[1] For example, low-pressure oxygen plasmas are used to modify wool surfaces by increasing tensile strength, abrasion resistance, and enhancing colorfastness. In biomedical technology, Menicon, a commercially available material used in contact lenses, is treated with O_2 plasmas to increase hydrophilicity.[2] Oxygen plasmas have also been employed in the synthesis of diamond and diamond-like films.[3]

During plasma processing, the sample is exposed to a complex reactive medium containing energetic species including ions, electrons, radicals, and UV/VUV radiation.[4] Within the discharge, the total flux of reactive neutrals and radicals produced are typically 3−4 orders of magnitude greater than the corresponding ion concentration.[5] Indeed atomic or molecular radicals are often cited as the key species responsible for initiating surface reactions during plasma processing.[6] Due to the wide range of reactive species within a plasma, however, the surface reactions of individual species are hard to determine.

The reactions of atomic oxygen, specifically $O(^3P)$, with different polymeric materials is also crucial in determining the performance and longevity of coatings used on spacecraft vehicles in Low Earth Orbit (LEO).[7−9] These coatings need to exhibit long-term stability[7] in order to survive the effects of ultraviolet radiation, thermal cycling, and an atmosphere comprised of 90% atomic oxygen observed at altitudes between 200 and 700 km.[8] In experiments by Golub et al.[10−12] the effect of $O(^3P)$ on a variety of polymeric substrates including poly(vinylidene fluoride) (PVDF), tetrafluoroethylene−ethylene copolymer (TFE-ET), and polyethylene (PE) was investigated by comparing structural and chemical changes, as well as etch rates in and out of the glow of a radio frequency O_2 plasma. These studies revealed substrate etching and a degree of surface oxidation that was less pronounced in the more fluorine-rich polymers.[10] For a given polymer, the degree of oxidation was also found to increase when the sample was placed in the plasma glow region. This result was attributed to the ion/O/O_2-rich effluent in the plasma glow compared to the O/O_2 rich region in areas removed from the plasma glow.[9,13]

A number of recent studies have explored the interaction of oxygen plasma treatments with self-assembled monolayers (SAMs). Clouet et al.[14] studied the effects of oxygen cold plasmas on hexatriacontane and octadecyl octadecanoate SAMs as models for the effects of plasmas on high-density polyethylene and polyester, respectively. Using mass spectrometry, they observed CO, H_2O, CO_2, and H_2 as the main gas-phase products during reaction with oxygen-rich plasmas. After a few minutes exposure, a steady-state distribution of gas-phase species was observed. The degradation of the SAM film was attributed to the action of atomic oxygen, while surface functionalization was attributed to the result of both atomic and molecular oxygen. Elms and co-workers followed the effect of O_2 plasmas on octadecyl mercaptan ($CH_3(CH_2)_{17}SH$) adsorbed on gold[9] and also concluded that there is a balance between substrate etching and oxidation. In contrast to Clouet et al.,[14] etching was attributed to the ions present in the plasma while oxidation was a result of reactions involving $O(^3P)$ and molecular oxygen. In a related study, Dai and co-workers studied the effects of different oxygen plasma components on an alkylthiolate SAM.[15] By filtering the plasma components using mesh and glass baffles, the effects of a full plasma treatment was compared to the plasma without ions and radiation. A much slower oxidation and etching rate was observed when ions and radiation were removed from the plasma discharge.

The present study focuses on the detailed interaction of atomic and molecular oxygen with an X-ray-modified hexadecane thiol adsorbed on gold SAM using in situ X-ray photoelectron spectroscopy. Atomic oxygen was generated by thermal dissociation of O_2, generating a mixture of $O(^3P)$ and O_2.[16] This approach was employed to identify the molecular level surface

* Author to whom correspondence should be addressed.

10.1021/jp0257350 CCC: $22.00
Published on Web 05/25/2002

reactions that accompany the interaction of atomic and molecular oxygen with hydrocarbon films without the interference of ions or radiation. This study also utilizes a number of important advantages that accrue from the application of thin organic films with well-defined structural properties as models for polymeric interfaces.[17] For instance, the use of SAMs greatly facilitates spectral analysis by reducing the background CC/CH_2 species in polyethylene.[10] Consequently, the nature and concentration of various O-containing species and their dependence on treatment time can be accurately determined. Furthermore, the ultrathin nature of the film also means that XPS can be employed to measure changes in the film's thickness under reaction conditions. In contrast to polymeric substrates, the surface temperature of a SAM can easily be controlled.[18,19] In the present study this advantage is exploited by carrying out reactions at low temperatures as a means to trap and probe volatile intermediates.

In the present study, the reaction of cross-linked hexadecanethiol/Au SAMs with O/O_2 was found to proceed in three distinct stages. Initially the incorporation of oxygen functionalities into the hydrocarbon film occurs in the absence of substrate erosion. At intermediate exposures, a steady-state distribution of C−O, C═O, and O−C═O species was observed in the film while CO and CO_2 desorption are responsible for erosion. Under these conditions, the limited penetration depth of oxygen radicals within the film results in pseudo zeroth-order kinetics associated with a constant carbon desorption rate. At longer exposures when the thickness of the film was reduced below the penetration depth of oxygen radicals, the loss of carbon exhibited pseudo first-order decay kinetics, accompanied by oxidation of sulfur and gold at the film/substrate interface.

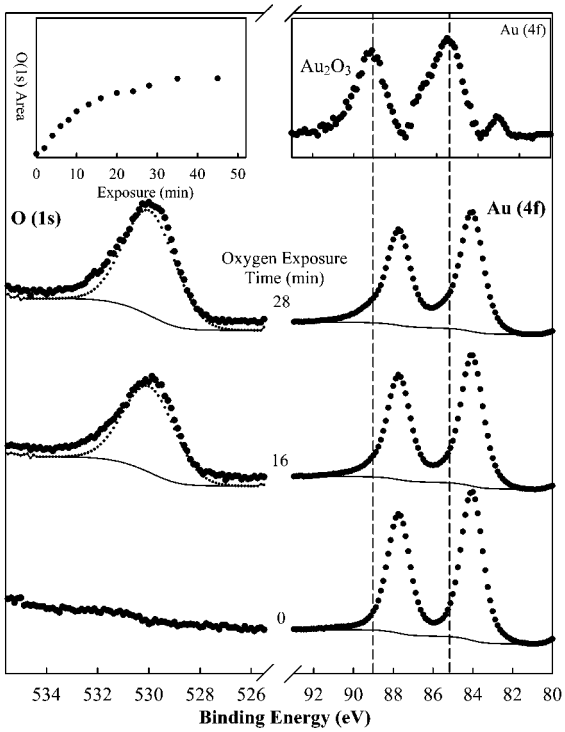

Figure 1. Variation in O(1s) and Au(4f) XPS regions for an Au sample exposed to the O/O_2 radical source as a function of time. Inset (top left) shows the variation of the O(1s) area as a function of O/O_2 exposure time. Inset (top right) shows the calculated Au(4f) XPS spectra of Au_2O_3. The dotted lines in the Au(4f) region indicate the peak positions of the $4f_{5/2}$ and $4f_{7/2}$ transitions associated with Au_2O_3.

Experimental Section

X-ray photoelectron spectroscopy (XPS) measurements were carried out in the same ultrahigh vacuum (UHV) chamber ($P_{base} \approx 5 \times 10^{-9}$ Torr) as the O/O_2 source. Details of the UHV system and associated capabilities can be found in a previous publication.[20] All XP spectra were collected at 15 kV and 300 W with a take-off angle of 45° from the sample normal. Unless otherwise noted, samples were mounted in a carousel stage with *xyz* translational and rotational capabilities. Binding energy scales were referenced to the CC/CH_2 peak in the C(1s) region at 284.6 eV.[15] XPS data fitting was performed using 100% Gaussian peaks. Shirley background subtraction was used in the Au(4f), C(1s), and O(1s) regions, while a linear background subtraction was employed in the S(2p) region.

Sample Preparation. Gold substrates were initially cleaned by Ar^+ ion sputtering and then dipped into a 5 mM solution of hexadecane thiol ($CH_3(CH_2)_{15}SH$) in ethanol for 10−12 h to prepare a C_{16}-SAM. Samples were then washed in ethanol, water, and hexanes and placed in the UHV carousel stage. C_{16}-SAMs (also referred to as hydrocarbon films) were subsequently treated with X-rays at 300 W for ≈15 h prior to O/O_2 exposure.

O/O_2 Source. Atomic oxygen was generated using a Thermal Gas Cracker TC-50 (Oxford Applied Research). This gas cracker works by dissociating molecular gases such as oxygen into a stream of atomic, low-energy reactive species. The gas, in this case molecular oxygen, passes through a metallic capillary heated by electron-beam irradiation and dissociates before entering the chamber. The tube is heated by electron emission from a heated filament, maintaining the capillary at a +2 kV relative to the filament. Electron bombardment heats the tube to ≈ 1000 °C; to avoid outgassing, the source is mounted inside a water-cooled copper block. The O/O_2 source is located in a line of sight with the sample (target-to-sample distance ≈ 5 cm). The O/O_2 source was operated at 30 W at a chamber pressure of $\approx 6 \times 10^{-7}$ Torr.

Low-Temperature Studies. Low-temperature studies were carried out in the same system but in these experiments, SAMs were mounted on a dedicated UHV manipulator (McAllister Technical Services) with capabilities for precision *xyz* translation, rotation, and sample cooling as well as direct heating capabilities. Samples were mounted on a tantalum foil that was attached to a ceramic feed-through coupled to the UHV manipulator. The sample was cooled by passing liquid nitrogen into a stainless steel tube connected to the ceramic feed-through, and the temperature monitored using an alumel−chromel thermocouple spot-welded to the back of the tantalum foil. The cooling system arrangement allowed sample temperatures of ≈100 K to be maintained.

Results

Figure 1 shows the O(1s) and Au(4f) XPS regions of a clean gold substrate that was sequentially exposed to the O/O_2 effluent from the radical source. Initially, no oxygen species were present in the O(1s) region, and the Au(4f) region is composed of a doublet at 84 and 87.6 eV corresponding to the $4f_{7/2}$ and $4f_{5/2}$ Au transitions, respectively. Figure 1 shows that, as the Au substrate is exposed to O/O_2, a new peak is observed in the O(1s) region at 529.7 eV.[21−23] Simultaneously, in the Au(4f) region, a decrease in intensity associated with the initial $Au4f_{7/2}$ and $4f_{5/2}$ doublet was observed as well as a broadening to the higher binding energy side. The resultant Au(4f) XPS region could be well fit by a combination of the initial $Au4f_{7/2}$ and

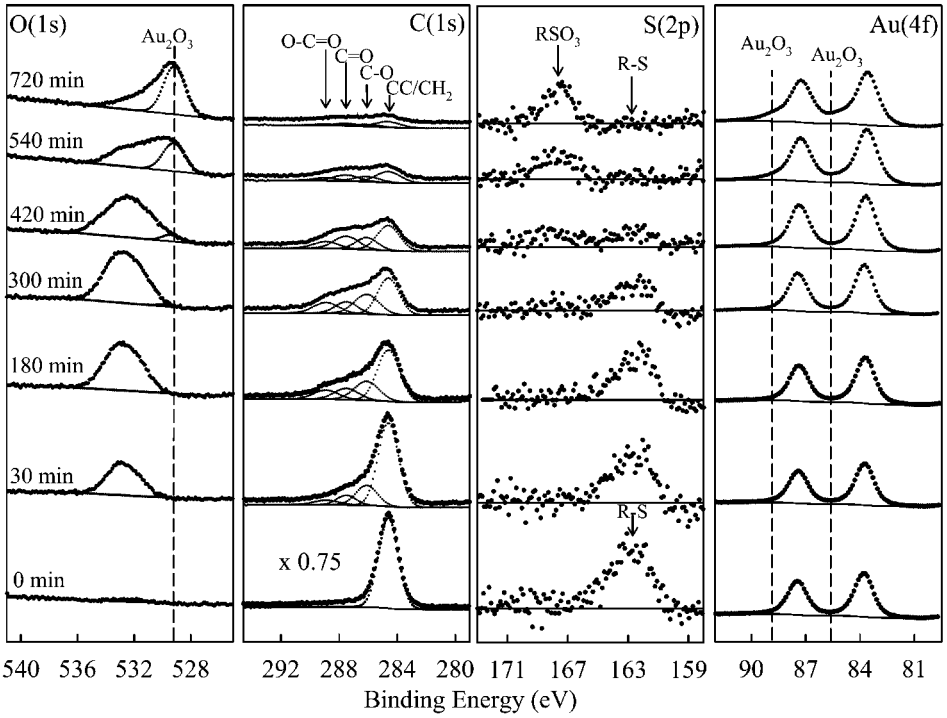

Figure 2. Variation in the O(1s), C(1s), S(2p), and Au(4f) XPS regions of the cross-linked C_{16}-SAM as a function of O/O_2 exposure time. The O(1s) region exhibits features centered at 532.7 eV and 529.9 eV, due to the various *O*−C species produced and Au_2O_3, respectively (the latter shown by a fitted dotted line). The C(1s) region was fit using a combination of CC/CH_2 (284.6 eV), *C*−O (286.1 eV), *C*═O (287.5 eV), and O−*C*═O (288.9 eV) species.[15] For each species, Gaussian peaks with a fwhm of 1.8−2.0 eV were employed. The S(2p) region exhibits two doublets centered at 162.8 eV and 168.0 eV due to native thiolate and sulfonate species, respectively. The Au(4f) region shows the $Au4f_{5/2}$ and $Au4f_{7/2}$ transitions of pure Au; the corresponding peaks due to Au_2O_3 are shown as dotted lines.

$4f_{5/2}$ doublet and a new $Au4f_{7/2}$ and $4f_{5/2}$ doublet with peaks centered at 85.5 eV and 89.1 eV, shown as a difference spectra in Figure 1 (insert: top right). Compared with previous studies on the UV/ozone oxidation of Au, these new $Au4f_{7/2}/4f_{5/2}$ and O(1s) peak positions are consistent with the formation of Au_2O_3.[23] In contrast, no change in the Au(4f) or O(1s) regions was observed upon exposure of a clean Au substrate to molecular oxygen.

The inset at the top left of Figure 1 shows the variation in the O(1s) XPS area associated with Au_2O_3 as a function of O/O_2 exposure. The Au_2O_3 signal can be seen to increase rapidly at short exposure times (<10 min) but saturates at exposure times greater than 20 min. On the basis of the attenuation of the $Au4f_{7/2}$ peak,[21,24] the thickness of the Au_2O_3 overlayer is estimated to be 7.3 Å.

Figure 2 shows the evolution of the O(1s), C(1s), S(2p), and Au(4f) XPS regions of an X-ray-modified hexadecanethiol SAM (C_{16}-SAM) adsorbed on gold, as the film is exposed to O/O_2. The initial X-ray irradiation initiates electron stimulated C−H, C−C, and S−Au bond breaking in the C_{16}-SAM,[25,26] generating a cross-linked carbonaceous overlayer, whose chemical composition is invariant to further X-ray irradiation. Pretreatment of the C_{16}-SAM was employed to minimize the effect of X-rays during subsequent XPS analysis of samples following exposure to the O/O_2 source. Consistent with this approach is the fact that the C(1s) XP spectral regions shown in Figure 2 were invariant to X-ray irradiation on the time scale of the spectral acquisition. Following X-ray exposure, the film exhibited a single peak in the C(1s) region at 284.6 eV corresponding to CC/CH_2 species and a featureless O(1s) region (Figure 2, t = 0 min).[15] The S(2p) region consists of a single doublet at 162.8 eV associated with the $2p_{3/2}$ and $2p_{1/2}$ transitions of native thiolate species bound to the underlying Au substrate.[9,15,25] The Au(4f) region is composed of two peaks at 84 eV and 87.6 eV due to the $4f_{7/2}$ and $4f_{5/2}$ transitions of metallic Au.

Upon initial exposure (<35 min) to O/O_2 (Figure 2, t = 30 min), there was a decrease in the *C*−C/*C*H_2 intensity in the C(1s) region, accompanied by a broadening of the overall spectral envelope to higher binding energies. This resultant C(1s) XPS envelope can be fit to a combination of CC/CH_2 (284.6 eV), *C*−O (286.1 eV), *C*═O (287.5 eV), and O−*C*═O (288.9 eV) species.[15] The appearance of these new oxygen-containing functionalities is also consistent with the appearance of a new broad peak in the O(1s) region centered at 532.7 eV, that can be ascribed to these various *O*−C species.[19] In contrast to the O(1s) and C(1s) regions, no changes are observed in the S(2p) and Au(4f) XPS regions during the initial exposure to O/O_2. At intermediate exposure times (60 < t < 420 min) the contribution of the *C*−O, *C*═O, and O−*C*═O groups in the C(1s) region, as well as the *O*−C peak in the O(1s) region, remain relatively constant although the *C*C/*C*H_2 peak intensity continues to decrease (Figure 2, 180 and 300 min). There are no noticeable changes in the S(2p) and Au(4f) region during this time, indicating that the O/O_2-induced transformations are restricted to the carbon-containing overlayer.

At longer exposure times (t > 420 min) the reaction trend observed by XPS changes drastically. For example at 420 min (Figure 2), the O(1s) region broadens to lower binding energies due to the appearance of a new feature at 529.9 eV, consistent with the formation of Au_2O_3. The formation of Au_2O_3 is also evidenced in the Au(4f) region by a broadening in the Au(4f) region similar to that observed in Figure 1 with a growth in intensity at 85.5 eV and at 89.1 eV due to the $4f_{7/2}$ and $4f_{5/2}$ transitions of Au_2O_3, respectively.[23] Simultaneously, the C(1s) region exhibits a decrease in the area of all species (*C*C/*C*H_2, *C*−O, *C*═O, and O−*C*═O). In the S(2p) region, the peak at

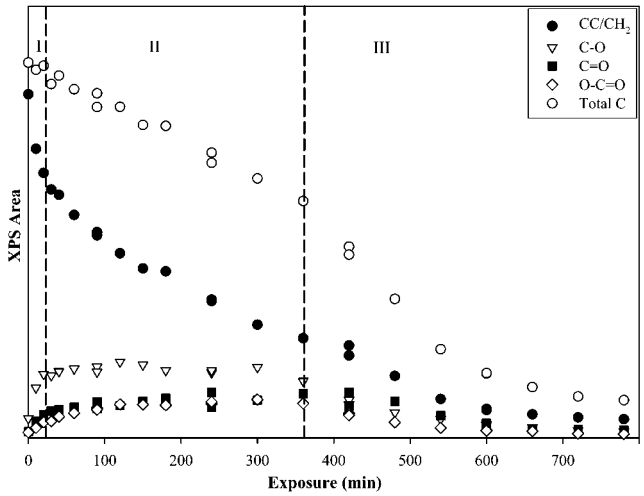

Figure 3. Variation in the XPS area associated with the CC/CH_2 (●) *C*−O (▽), *C*═O (■), and O−*C*═O (◇) species as well as the total carbon signal (○) as a function of O/O_2 exposure time. The three stages of the reaction are delineated by dotted lines.

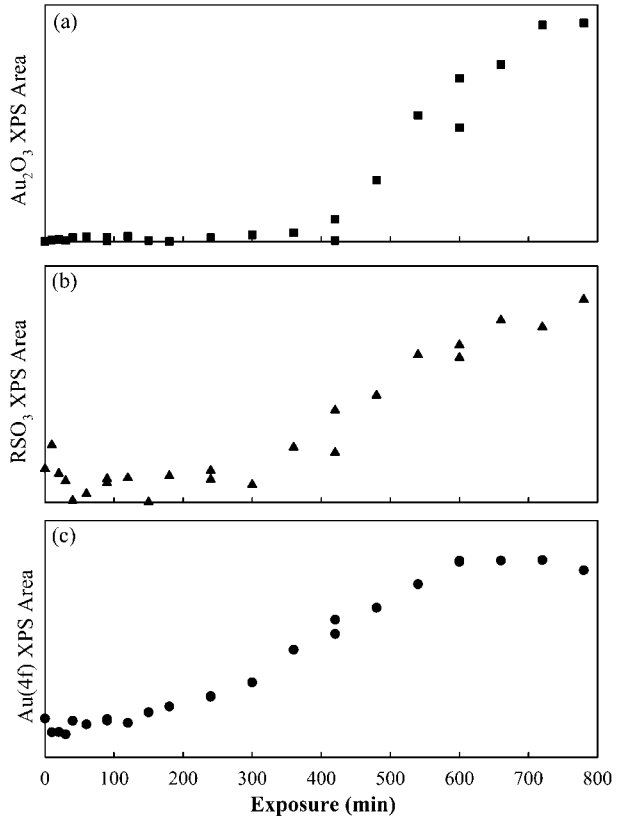

Figure 4. Time-dependent variation in XPS area of (a) Au_2O_3─calculated from the area of the O(1s) peak observed at 529 eV (b) sulfonate (RSO_3) species─calculated from the peak centered at 168 eV in the S(2p) region, and (c) substrate Au signal─ calculated from the total Au(4f) XPS signal. The data presented in this figure are compiled from a data set that includes the spectra presented in Figure 2.

162.8 eV associated with native thiolate species begins to decrease accompanied by the appearance of a new peak at 168.0 eV consistent with the production of sulfonate (RSO_3) species.[15,19] At even longer O/O_2 exposures (Figure 2, 540 and 720 min), the formation of Au_2O_3 becomes more evident, while intensity associated with carbon-containing species continues to decrease, and the S(2p) region now consists of a single peak associated with RSO_3 groups. It should be noted that in contrast

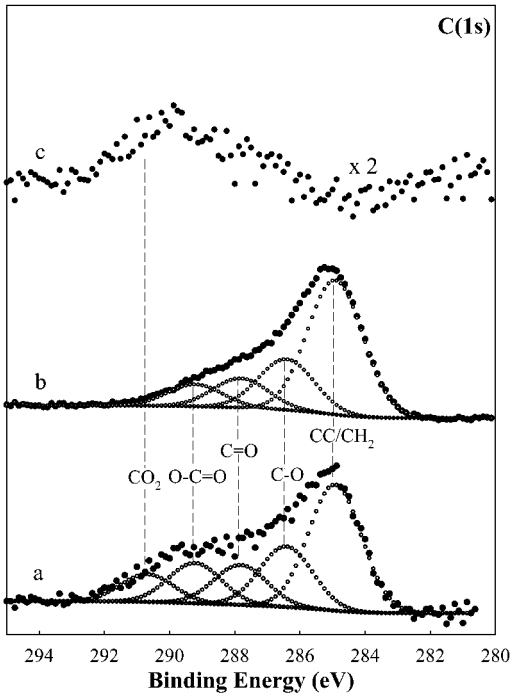

Figure 5. (a) The C(1s) XPS region of the cross-linked C_{16}-SAM after 3 h of radical exposure with the substrate held at 113K. (b) The corresponding XPS of the cross-linked C_{16}-SAM seen in part (a) after the substrate is annealed to 298 K. (c) The difference spectra of (a) and (b). The raw XPS data are shown as filled circles while fits for the CH_2/CC, C−O, C═O and O−C═O groups are shown as open circles. It should be noted that samples held at 113 K for several hours without exposure to the O/O_2 source did not exhibit any change in the C(1s) region due to CO_2 adsorption from the background.

no chemical changes were observed when modified C_{16}-SAMs were exposed to molecular oxygen for several hours.

Figure 3 shows the area of the *C*C/*C*H_2 (284.6 eV), *C*−O (286.1 eV), *C*═O (287.5 eV), and O−*C*═O (288.9 eV) species in the C(1s) region as well as the total carbon signal as a function of O/O_2 exposure time compiled from the data set containing the spectra shown in Figure 2. The changes observed in the C(1s) region can be divided into three separate regions, as shown in Figure 3. In region (I) (0 min < t < 35 min) oxygen-containing carbon functionality appears in the film. Of the oxygen-containing functionality produced, C−O species are produced in the greatest abundance while the time dependence and concentration of C═O and O−C═O groups are very similar to one another. During this time period, the CC/*C*H_2 species experience a rapid decrease in area (28% loss in signal after 30 min O/O_2 exposure) while the total C(1s) area remains constant. In region II (60 min < t < 360 min) the growth of C−O, C═O, and O−C═O reaches a steady state although the total C(1s) signal decreases linearly with O/O_2 exposure. In region III (t > 360 min) the area of the C−O, C═O, and O−C═O species begin to decrease. Figure 3 also shows that the loss in total carbon signal as a function of O/O_2 exposure in this region follows a more rapid exponential like decay compared to the linear dependence observed in region II. Although no attempt was made to systematically study pristine, nonirradiated C_{16}-SAMs due to the effect of X-ray irradiation on the film's carbon content a few selected experiments indicated that the evolution of the C(1s) region as a function of exposure to the O/O_2 source was qualitatively similar to those observed on the cross-linked C_{16}-SAMs.

Figure 4 shows the variation in area of the Au_2O_3, RSO_3, and total Au as a function of O/O_2 exposure time. Figure 4, a

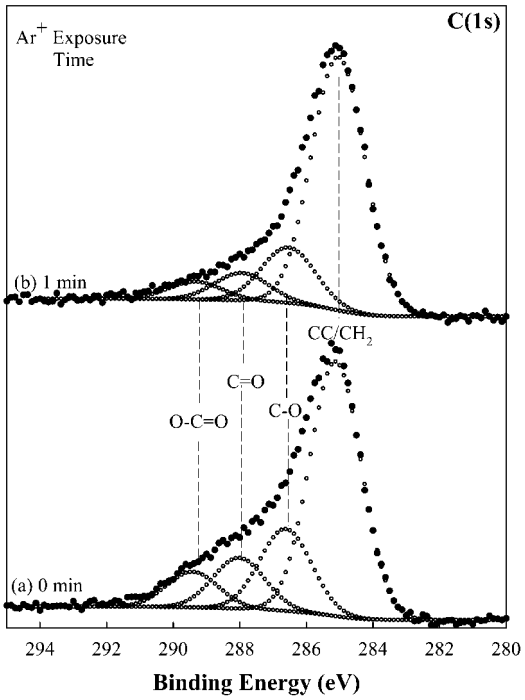

Figure 6. Comparison of the C(1s) XPS region after 2 h exposure to the O/O_2 source (a) and then after 1 min of Ar^+ ion sputtering (b). ($E_{Ar^+} = 2$ keV). The raw XPS data are shown as filled circles while fits for the CH_2/CC, C−O, C═O, and O−C═O groups are shown as open circles. The C(1s) spectra have been normalized to the area of the CC/CH_2 peak.

and b, can be seen to exhibit a very similar dependence upon O/O_2 exposure, with Au_2O_3 and RSO_3 only appearing after ≈420 min and then increasing with exposure time. Figure 4c shows that the Au XPS signal remains virtually unchanged at low exposure times (t < 120 min). Between 120 and 600 min of O/O_2 exposure, the Au(4f) signal increases, reaching a maximum value after ≈600 min.

Figure 5 shows the result of separate experiments carried out on a cross-linked C_{16}-SAM cooled to 113 K. Figure 5a shows the C(1s) region following exposure to the O/O_2 source for 3 h at 113 K. The C(1s) region was fitted with the same CC/*C*H_2, *C*−O, *C*═O, and O−*C*═O peaks, parameters, and positions used in Figure 2. An additional peak, centered at 290.3 eV, however, was also required to adequately fit the C(1s) spectral envelope. The substrate was then heated to room temperature and the C(1s) XPS reacquired (Figure 5b). A comparison of Figure 5, a and b, indicates that the main difference between these spectra is that intensity associated with the higher binding energy feature has been lost upon annealing to room temperature. This is illustrated by the difference spectra between the low- and room-temperature XP spectra shown in Figure 5c.

Figure 6 shows the difference in the C(1s) spectra of a cross-linked C_{16}-SAM treated with O/O_2 for 120 min before (Figure 6a) and after (Figure 6b) Ar^+ ion sputtering. Following O/O_2 treatment of the cross-linked C_{16}-SAM (Figure 6a) C−O, C═O, and O−C═O groups are detected in the film, consistent with the results presented in Figure 2. Subsequent Ar^+ ion sputtering of the film produced a decrease in the total C(1s) signal (not shown). Furthermore, the C(1s) envelope exhibited a significant decrease in the relative contribution from oxygen-containing carbon functionality (represented by the area of the C−O, C═O, and O−C═O groups) compared to CC/CH_2 species (cf. Figure 6, a and b). It should be noted that in order to provide a direct comparison of the distribution of carbon-containing functionality, the C(1s) spectra in Figure 6 have been normalized to the CC/CH_2 peak area.

SCHEME 1: Schematic of the Interaction of O/O_2 with a C_{16}-SAM Modified by X-ray Irradiation[a]

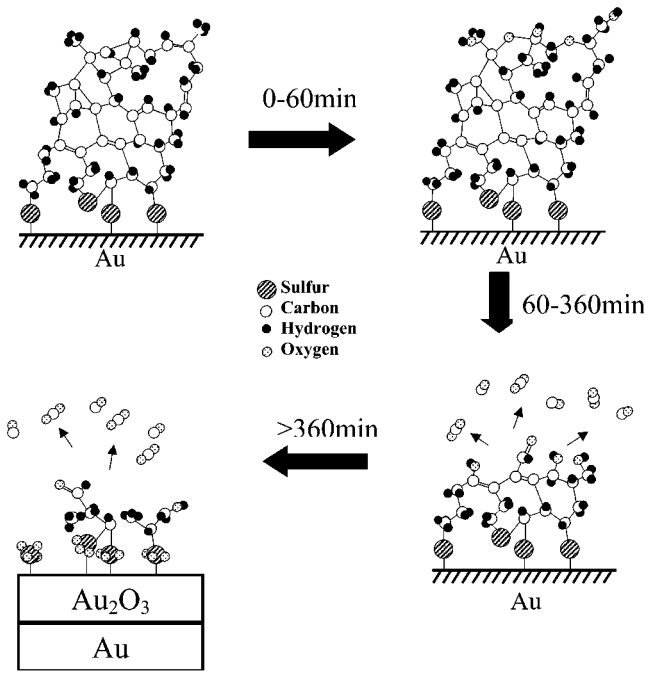

[a] Reaction steps include the incorporation of oxygen-containing functionality into the hydrocarbon film, erosion of the carbonaceous overlayer, and oxidation of sulfur and gold species present at the substrate/film interface. The initial structure of the C_{16}-SAM after X-ray irradiation is based on information contained in refs 25,26,39.

Discussion

Source Calibration. Figure 1 illustrates that the passage of molecular oxygen through the thermal cracker leads to the uptake of oxygen on the Au substrate and the production of a thin Au_2O_3 overlayer. Evidence of a surface limited reaction is supported by the rapid uptake of oxygen at short exposures before a saturation coverage is reached at longer exposures (Figure 1: insert). In summary, the information contained in Figure 1 is taken as evidence for the production of atomic oxygen when the tube is heated based on the subsequent production of Au_2O_3 through the reaction:

$$Au(s) + O(g) \rightarrow Au_2O_3(s)$$

Consequently, the effluent from the heated source can be considered a mixture of atomic and molecular oxygen ($O(^3P)/O_2$).[16]

Interaction of O/O_2 with the Hydrocarbon Overlayer. The results presented in Figures 2−6 allow us to develop a detailed understanding of the molecular level events that accompany the interaction of O/O_2 with hydrocarbon films. These are shown schematically in Scheme 1 as a function of O/O_2 exposure time.

Stage I. Figure 3 shows that the reaction of O/O_2 with the X-ray modified C_{16}-SAM can be divided into three distinct regions. At very short exposures (stage I) oxygen functionality in the form of C−O, C═O, and O−C═O is introduced into the hydrocarbon film. During this time regime there is little or no change in the total carbon content although the CC/CH_2 peak area decreases markedly. Based on previous studies, the initial reaction of oxygen radicals with hydrocarbon films involves H-abstraction leading to the production of •OH radicals in the

gas phase and the production of alkyl radicals in the hydrocarbon film thus (Scheme 1):[14,27−30]

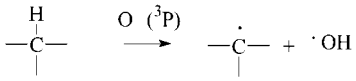

The subsequent formation of oxygen containing functional groups (R−O−R, C═O, and O−C═O species) is postulated to occur via peroxyradicals formed by the reaction of singlet state oxygen with alkyl radicals.[14,28−30] For example:

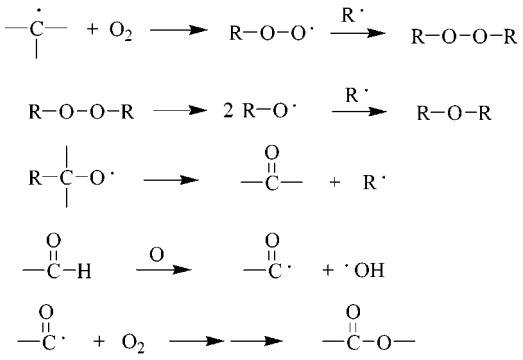

Since the production of oxygen-containing functionality will be controlled by the effective diffusion length of oxygen atoms within the hydrocarbon film, R−O−R, C═O, and O−C═O species are expected to be localized at the vacuum/film interface. This hypothesis is supported by results of Ar^+ ion sputtering carried out in conjunction with XPS (Figure 6). The decrease in concentration of C−O, C═O, and O−C═O species compared to the CH_2/CC groups observed after 1 min of Ar^+ ion sputtering, reveals that in O/O_2-modified films, the majority of oxygen-containing functionality is present at the film/vacuum interface, consistent with previous studies of $O(^3P)$ reactions with organized ultrathin hydrocarbon films.[19]

The fact that the total carbon content, measured by the integrated area of the C(1s) peak, is virtually unchanged in stage I while the CC/CH_2 peak decreases significantly indicates that during this early time period, reactions are dominated by the incorporation of new oxygen-containing functionality and that erosion of the hydrocarbon film has yet to be initiated. This assertion is also supported by the constant Au(4f) XPS signal associated with the underlying substrate during stage I (Figure 4c).

Stage II. During stage II, erosion of the hydrocarbon film is initiated. This is evidenced by the decrease in the total carbon signal and a concomitant increase in the Au(4f) XPS signal. Figure 3 illustrates that during this period, the C−O, C═O, and O−C═O concentration remains virtually unchanged and the loss in total carbon signal is due almost exclusively to the loss of CC/CH_2 species, consistent with the formation of a steady-state "erosion front" (Scheme 1). The loss of carbon from the film is ascribed to the formation of volatile CO and CO_2 species through reactions such as:[31]

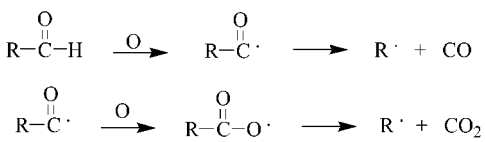

Furthermore, Figure 3 shows that erosion of the film, evidenced by the decrease in total carbon content, is initiated only after a steady-state composition of oxygen-containing carbon functionality is attained. This supports the idea that the generation of oxygen-containing carbon functionality is a necessary precursor for etching.

The production of CO_2 as a volatile species is supported by results obtained when the hydrocarbon film is subject to reactions with O/O_2 while the sample temperature is held at 113 K (Figure 5). Under these low-temperature conditions CO_2 is expected to remain physisorbed (ΔH_{vap} (CO_2) = 26.1 kJ mol^{-1})[32] while CO is still released as a gas-phase product due to its greater volatility (ΔH_{vap} (CO) = 6 kJ mol^{-1}).[32] Figure 5 shows that the C(1s) envelope produced during O/O_2 reactions at these low surface temperatures is broadened to higher binding energies compared to analogous experiments carried out at room temperature (Figure 2) requiring the inclusion of an additional carbon component centered at 290.3 eV, consistent with the higher binding energy anticipated for CO_2 compared to R−O−R, C═O, or O−C═O species.[33] Upon annealing the surface to room temperature this high binding energy component disappears (Figure 5, b and c) indicative of the volatile nature of these CO_2 species.

On the basis of the reaction mechanism outlined in stage I and the relative rate constants for hydrogen abstraction and subsequent peroxyl radical formation, the rate-determining step for carbon loss from the film is expected to be the initial hydrogen abstraction step mediated by oxygen radicals.[27,34,35] Under these conditions the overall reaction rate can be expressed as:

$$\text{rate of carbon loss} = k[\text{CH}][\text{O}]$$

where [CH] and [O] represent the concentration of C−H groups and oxygen radicals, respectively. The flux of O radicals striking the surface is held constant by maintaining a constant operating temperature of the source and the O_2 flow rate through the tube. Consequently, the constant rate of carbon loss in Stage II, characteristic of a zeroth-order reaction rate, indicates that [CH] is constant in this time regime. This phenomena is a consequence of the fact that at any given time, only carbon atoms close to the film/vacuum interface are involved in reactions with incoming O/O_2 species, consistent with oxygen-containing carbon functional groups being localized at the film/vacuum interface (Figure 6). Thus, the [CH] referred to in eq 1 is really a measure of CH group concentration in the near surface region ($[CH]_{surface}$). On the basis of the absence of products associated with O atom reactions at the film/substrate interface (Au_2O_3 and RSO_3^-—see Figures 2 and 4), the average penetration depth of O atoms within the hydrocarbon film is less than the film's total thickness during stage II. Consequently, the $[CH]_{surface}$ is expected to remain constant giving rise to the constant rate of carbon loss observed. Scheme 1 illustrates that under room-temperature conditions, CO_2 and CO desorb from the film and reveal underlying hydrocarbon layers, thereby sustaining the etch process. It should be noted that the observation of zeroth-order kinetics in the present investigation is in contrast to the pseudo first-order kinetics reported for the loss of methyl (CH_3) and methylene (CH_2) groups during the reaction between $O(^3P)$ and a LB film of cadmium arachidate $(CH_3(CH_2)_{18}COO^-)_2Cd^{2+}$ on silicon, measured by FTIR.[19]

Efficiency of O Atom Etching. The efficiency of O etching within the hydrocarbon film can be estimated from knowledge of the O atom flux and the loss in film thickness during stage II. The O atom flux can be determined from information contained in Figure 1 utilizing the fact that XPS can provide quantitative information on changes in the thickness of an

overlayer. The attenuation of the $Au4f_{7/2}$ signal observed in Figure 1 enables us to determine that the Au_2O_3 overlayer is initially increasing at a rate of 0.29 Å/min. A single Au_2O_3 monolayer is expected to produce an 8.0 Å thick overlayer based on the unit cell dimensions.[36] Taken in conjunction with the initial sticking probability of atomic oxygen on clean Au (5×10^{-3}) previously calculated by Wanner et al.,[37] the growth rate of the Au_2O_3 overlayer indicates that the constant flux of O atoms generated by the source per minute is ≈ 22 per unit cross-sectional area.

The reduction in hydrocarbon film thickness during stage II can be estimated from the increase in Au(4f) XPS signal (Figure 4c) using the inelastic mean free path of 34 Å calculated for Au(4f) photoelectrons in self-assembled monolayers.[38] Results from this analysis indicate that the hydrocarbon film thickness is reduced by 5.4 Å in 330 min. Since the XPS analysis region is the same in Figures 1 and 2 the total cross-sectional area will be identical. This enables us to calculate that the hydrocarbon film thickness is reduced with an efficiency of $\approx 7.4 \times 10^{-4}$ Å/incident O atom. On the basis of the approximations inherent in this calculation, we consider that this value is accurate to within an order of magnitude.

Stage III. Upon prolonged O/O_2 exposures (in excess of $\approx$ 350 min) erosion of the film is still observed although the reaction kinetics are different from stage II. In stage III, O atoms are able to penetrate to the film/substrate interface evidenced by the simultaneous appearance of RSO_3 and Au_2O_3 in the S(2p) and Au(4f) XPS regions (Figure 4, a and b), respectively (Scheme 1). Furthermore, the change in the S(2p) XPS area in this time region the interaction of atomic oxygen with sulfur appears to be dominated by oxidation rather than desorption.

Figure 3 shows that in stage III the loss of carbon from the film is characterized by a first-order decay process. This is a reflection of the fact that although the O/O_2 flux is still constant, the depth of O atom penetration within the film is on the same length scale or greater than the thickness of the remaining hydrocarbon overlayer. Under these conditions the [CH] is no longer constant, leading to the pseudo first-order kinetic behavior evidenced in Figure 3. Similarly the concentration of R−O−R, C═O, and O−C═O groups decreases as the concentration of CH moieties accessible to incoming O atoms is reduced.

The effective diffusion length of oxygen radicals in the film can be estimated from the thickness of the hydrocarbon film at the point where oxidation of the film/vacuum interface occurs, the latter based on the appearance of Au_2O_3 and RSO_3 species. Such an analysis reveals that the effective diffusion length (or penetration depth) of atomic O within the hydrocarbon film is $\approx$5.5 Å. Furthermore, the fact that Au_2O_3 and RSO_3 species are not observed until after prolonged O/O_2 exposure indicates that although X-ray irradiation of SAMs induces carbon, sulfur, and hydrogen desorption[25,26] the X-ray-modified C_{16}-SAM forms a 3-dimensionally dense overlayer, preventing O-atom penetration to the film/vacuum interface (Scheme 1). These results are consistent with those of George et al. [9] who found that carbon oxidation and C−C bond cleavage occur prior to oxidation at the film/substrate interface. In a broader sense we also believe that the three stages of reaction outlined in the present investigation will be generally relevant to oxygen atom etching of hydrocarbon films and carbonaceous material although it should be noted that for thicker films the relative importance of stage II (constant etching) will increase.

Conclusions

The reaction of a mixture of atomic and molecular oxygen with a well-defined organic thin film initially proceeds via H-abstraction at the vacuum/film interface to produce an alkyl radical. These species react rapidly with molecular oxygen to produce a peroxyradical whose subsequent chemistry leads to the formation of R−O−R, C═O, and O−C═O species. Once a steady-state distribution of oxygen-containing carbon functionality has been established, removal of carbon from the film (etching) proceeds via the formation of volatile species, including carbon dioxide. Under these conditions, a zeroth-order loss of carbon from the film is observed due to the fact that the effective diffusion length of oxygen radicals in the film is less than the thickness of the hydrocarbon film. At longer O/O_2 exposures oxidation of the vacuum/film interface occurs producing Au_2O_3 and sulfonate (RSO_3) species. Under these conditions carbon loss from the film exhibits pseudo first-order kinetics due to the limited thickness of the remaining overlayer.

Acknowledgment. Support for this research was provided by a National Science Foundation CAREER award (No. 9985372) and a grant from the Petroleum Research Fund (PRF No. 35281-G5, G6) administered through the American Chemical Society.

References and Notes

(1) Dai, X. J.; Hamberger, S. M.; Bean, R. A. *Aust. J. Phys.* **1995**, *48*, 939.
(2) Fawkes, D. W.; Davis, M. C.; Brown, A.; Newton, J. M. *Surf. Interface Sci.* **1998**, *13*, 233.
(3) Joshi, A.; Nimmagadda, R. *J. Mater. Res.* **1991**, *6*, 1484.
(4) Lieberman, M. A.; Lichtenberg, A. J. *Principles of Plasma Discharges and Materials Processing*; John Wiley & Sons: New York, 1994.
(5) Cahn, M.-C.; Ko, T.-M.; Hiraoka, H. *Surf. Sci. Rep.* **1996**, *24*, 1.
(6) Kuppers, J. *Surf. Sci. Rep.* **1995**, *22*, 249.
(7) Ngo, T.; Snyder, E. J.; Tong, W. M.; Williams, R. S.; Anderson, M. S. *Surf. Sci.* **1994**, *314*, L817.
(8) Bourdon, E. B. D.; Raveh, A.; Gujrathi, S. C.; Martinu, L. *J. Vac. Sci. Technol. A* **1993**, *11*, 2530.
(9) Elms, F. M.; George, G. A. *Polym. Adv. Technol.* **1998**, *9*, 31.
(10) Golub, M. A.; Cormia, R. D. *Polymer* **1989**, *30*, 1576.
(11) Golub, M. A. *Makromol. Chem., Macromol. Symp.* **1992**.
(12) Golub, M. A.; Wydeven, T.; Cormia, R. D. *Langmuir* **1991**, *7*, 1026.
(13) Golub, M. A.; Wydeven, T. *Polym. Degrad. Stab.* **1988**, *22*, 325.
(14) Clouet, F.; Shi, M. K. *J. Appl. Polym. Sci.* **1992**, *46*, 1955.
(15) Dai, X. J.; Elms, F. M.; George, G. A. *J. Appl. Polym. Sci.* **2001**, *80*, 1461.
(16) Herzberg, G. *Spectra of Diatomic Molecules*; D. Van Nostrand Company, Inc.: Princeton, NJ, 1967.
(17) Perry, C. C.; Carlo, S. R.; Wagner, A. J.; Vecitis, C.; Torres, J.; Kolegraff, K.; Fairbrother, D. H. Self-assembled Monolayers as Models for Polymeric Interfaces. In *ACS Symposium on "Solid Surfaces and Thin Films"*; Soriaga, M., Ed.; American Chemical Society: Washington, DC, 2002.
(18) Dubois, L. H.; Zegarski, B. R.; Nuzzo, R. G. *J. Am. Chem. Soc* **1990**, *112*, 570.
(19) Paz, Y.; Trakhtenberg, S.; Naaman, R. *J. Phys. Chem.* **1994**, *98*, 13517.
(20) Perry, C. C.; Torres, J.; Carlo, S.; Fairbrother, D. H. *J. Vac. Sci. Technol. A*, submitted.
(21) Yan, C.; Gölzhäuser, A.; Grunze, M.; Wöll, C. *Langmuir* **1999**, *15*, 2414.
(22) Canning, N. D. S.; Outka, D.; Madix, R. J. *Surf. Sci.* **1984**, *141*, 240.
(23) Krozer, A.; Rodahl, M. *J. Vac. Sci. Technol. A* **1997**, *15*, 1704.
(24) King, D. E. *J. Vac. Sci. Technol. B* **1995**, *13*, 1247.
(25) Wagner, A. J.; Carlo, S.; Vecitis, C.; Fairbrother, D. H. *Langmuir* **2000**, *18*, 1542.
(26) Wirde, M.; Gelius, U.; Dunbar, T.; Allara, D. L. *Nucl. Instrum. Methods Phys. Res.* **1997**, *131*, 245.
(27) Ausfelder, F.; McKendrick, K. G. *Prog. React. Kinet. Mechanisms* **2000**, *25*, 299.
(28) Lianos, L.; Parrat, D.; Hoc, T. Q.; Duc, T. M. *J. Vac. Sci. Technol. A* **1994**, *12*, 2491.
(29) Kill, G.; Hunter, D. H.; Mcintyre, N. S. *J. Polym. Sci. A* **1996**, *34*, 2299.
(30) Garton, D. J.; Minton, T. K. *J. Chem. Phys.* **2000**, *112*, 5975.

(31) Fossey, J.; Lefort, D.; Sorba, J. *Free Radicals in Organic Chemistry*; John Wiley & Sons: New York, 1995.
(32) *CRC Handbook of Chemistry and Physics*, 75th ed.; CRC Press Inc.: Boca Raton, FL, 1994.
(33) Onishi, H.; Egawa, C.; Aruga, T.; Iwasawa, Y. *Surf. Sci.* **1987**, *191*, 479.
(34) Hippler, H.; Troe, J.; Willner, J. *J. Chem. Phys.* **1990**, *93*, 1761.
(35) Cruz, G. *J. Comput. Chem.* **1999**, *20*, 845.
(36) Schwarzmann, E.; Mohn, J.; Rumpel, H. *Z. Naturforsch.* **1976**, *31b*, 135.
(37) Linsmeier, C.; Wanner, J. *Surf. Sci.* **2000**, *454*−*456*, 305.
(38) Bain, C. D.; Whitesides, G. M. *J. Phys. Chem.* **1989**, *93*, 1670.
(39) Zharnikov, M.; Geyer, W.; Golzhauser, A.; Frey, S.; Grunze, M. *Phys. Chem. Chem. Phys.* **1999**, *1*, 3163.